The Cryosphere, 20, 6071–6086, 2026
https://doi.org/10.5194/tc-20-6071-2026
© Author(s) 2026. This work is distributed under
the Creative Commons Attribution 4.0 License.

The Cryosphere Open Access EGU

Progressive changes in geometry and dynamics of the Northern Pine Island Ice Shelf, West Antarctica

Yite Chien[1,2,3,4], **Chunxia Zhou**[1,2,3], **and Baojun Zhang**[1,2,3]

[1]Chinese Antarctic Center of Surveying and Mapping, Wuhan University, Wuhan, 430079, China
[2]Key Laboratory of Polar Environment Monitoring and Public Governance (Wuhan University), Ministry of Education, Wuhan, 430079, China
[3]School of Geodesy and Geomatics, Wuhan University, Wuhan, 430079, China
[4]Center for Space and Remote Sensing Research, National Central University, Zhongli, Taoyuan 320317, Taiwan

Correspondence: Chunxia Zhou (zhoucx@whu.edu.cn)

Received: 16 January 2026 – Discussion started: 30 January 2026
Revised: 21 August 2026 – Accepted: 6 October 2026 – Published: 21 October 2026

Abstract. The Pine Island Ice Shelf can be analysed within three distinct sectors: northern, southern, and central. Dynamics within the Northern Pine Island Ice Shelf (N-PIIS) remain less understood than those of the Central Pine Island Ice Shelf. Using satellite imagery and data, we investigate changes in the N-PIIS, including ice-front position and pinning-point evolution since 1973, annual ice velocity since 2014, surface elevation since 2018, rift propagation events in 2022 and 2025, and polynya activity from 1986 to 2026. Our results show an overall reduction in ice-shelf area, with increased calving following the loss of pinning points and reduced protection by landfast sea ice against ocean swell. Velocities of grounded and floating ice have increased. Polynya formation within the ice shelf may promote disconnection from the ice sheet and reduce lateral buttressing. Surface elevation changes and the redistribution of pinning points indicate ongoing thinning. Newly formed rifts are likely to promote further calving events. Our observations document continued thinning, frontal retreat, pinning-point loss, and rift propagation at the N-PIIS. This study provides critical new insights into the evolving stability of the N-PIIS and highlights the importance of continued monitoring to anticipate potential disintegration.

1 Introduction

The Pine Island Ice Shelf (PIIS) is one of the most dynamically active ice shelves in West Antarctica and plays a critical role in regulating ice discharge from the Pine Island Glacier basin (Joughin et al., 2021). Previous studies have shown that changes in ice-shelf geometry, grounding, and basal melting strongly influence glacier acceleration and mass loss in this region (Rignot, 2002; Dutrieux et al., 2014). The PIIS is commonly divided into northern, central, and southern sectors, which differ markedly in flow speed, basal melt rates, and buttressing strength (Schmeltz et al., 2001; Rignot, 2002).

Compared with the rapidly thinning and fast-flowing central and southern sectors, the northern PIIS (N-PIIS) has received relatively little attention. The N-PIIS is characterized by slower ice motion and is primarily fed by the Larter, Lucchitta, and Velasco Glaciers (Fig. 1a). Over recent decades, the region has experienced substantial frontal retreat. The ice-shelf area decreased by 13.3 % in 1992 (relative to 1966), 16.7 % in 1996, and 27.2 % in 2000, with the 1996–2000 reduction being three times that of 1992–1996, indicating an accelerating retreat rate (Rignot, 2002). A major calving event in 2015 disconnected it from the central PIIS (Arndt et al., 2018). Despite this retreat, the grounding line has remained relatively stable at the Lucchitta and Larter glaciers, which are situated on a more pronounced, mountainous, and prograde bed topography (Andersen et al., 2026). However, most pinning-point areas across the N-PIIS decreased between 1973 and 2022, according to Miles and Bingham (2024), indicating ice-shelf thinning (Fig. 1a).

These observations raise the question of whether processes similar to those reported by Walker et al. (2024) and Teder et al. (2025) are also active at the N-PIIS. These studies documented ice-shelf thinning, loss of pinning points, and enhanced fracturing at the Conger–Glenzer, Wilkins, and Voyeykov ice shelves, occurring alongside regional sea ice decline and increased ocean-swell exposure, and preceding rapid rift propagation and ice-shelf collapse. Whether a similar sequence of changes is occurring at the N-PIIS remains unclear.

To address this, we present an observation-based analysis of recent dynamic changes of the N-PIIS. Rather than attributing changes to a single forcing mechanism, we document co-evolving ice-front retreat, grounding conditions, thinning signals, and polynya occurrence. We focus on the key phenomena that related to rapid collapse event, including the ice front retreat, the evolution of rifting and pinning points, and the changes of landfast sea ice. Together, these observations provide new insights into the evolving changes of the N-PIIS.

2 Data and Methods

2.1 Ice-front position, rift propagation, and polynya mapping

Landsat and Sentinel-1/2 imagery accessed via USGS EarthExplorer, the Copernicus Browser, and Google Earth Engine were used to analyse ice-front position changes, rift propagation, and polynya formation at the N-PIIS.

To characterize the overall changes in the ice-front position of the N-PIIS, we extracted ice-front positions from 1973–1998 using Landsat-1 MSS Collection 2 Level 1 imagery (60 m spatial resolution) and Landsat-4/5 TM Collection 2 Level 1 imagery (30 m spatial resolution) downloaded from USGS EarthExplorer platform. The imagery was first geometrically corrected, and the RGB bands were composited to generate true-color images for subsequent manual delineation of the ice-front. From 1999–2026, ice-front positions were extracted through manual visual interpretation using Landsat-7/8/9 Collection 2 TOA panchromatic imagery (15 m spatial resolution) and Sentinel-1 IW GRD imagery (10 m spatial resolution) on the Google Earth Engine platform.

The overall extraction uncertainty was estimated as ± 1 pixel. Ice-front positions from 1973–1998 were derived from Landsat-1/4/5 imagery, with uncertainties of ±60 m for Landsat-1 and ±30 m for Landsat-4/5, whereas positions from 1999 to October 2014 were derived from Landsat-7/8/9 imagery, with an uncertainty of ±15 m. From October 2014–2026, Sentinel-1 IW GRD imagery was used to obtain ice-front positions during the polar night, with an uncertainty of ±10 m. To ensure consistency between the ice-front positions derived from different sensors, Landsat and Sentinel-1 imagery acquired during their overlapping observation period were compared and cross-checked, with particular attention paid to observations acquired at similar times.

Changes in ice-front position were quantified relative to a reference ice-shelf mask. Ice-shelf masks for N-PIIS1, N-PIIS2, and N-PIIS3 (Fig. 1) were defined using the 2011 grounding line (Rignot et al., 2016) and were extended beyond the observed ice-shelf extent to ensure complete capture of frontal variation. The boundaries that separated ice shelf mask is based on the position of the pinning points. Percentage area loss for each observation was calculated relative to the maximum area in the full time series.

Landsat-1 optical imagery (60 m) and Landsat-4/5/7/8/9 optical imagery (30 m) from Google Earth Engine, Sentinel-2 optical imagery (10 m) and Sentinel-1 SAR imagery (10 m) from the Copernicus Browser, were used to manually identify calving events during the 2025/2026 austral summer, rift propagation in 2022 and 2025, and manually identify polynya evolution from 1986–2026.

2.2 Ice velocity

Annual composite ice-velocity data (2014–2026) were obtained from the ITS_LIVE web map interface (https://its-live.jpl.nasa.gov/app/index.html; last access: April 2026), which enables interactive exploration of glacier velocity time series at any location on earth (Fahnestock and Dow, 2023; Gardner et al., 2025). Users can query geographic coordinates or select points on a map to retrieve full velocity records at specified locations. Annual composite velocities were extracted following the method of Gardner et al. (2025), in which all input velocity data are first smoothed using a 15-point moving window filter. A coefficient matrix is then constructed to represent the fractional contribution of each image pair to individual years, allowing least-squares estimation of annual mean velocities. Weighting is defined as the inverse square of displacement uncertainty (velocity error × time interval), and annual velocities are derived from an error-weighted least-squares fit of all valid observations.

Time series of annual composite velocity were extracted at nine locations (N1–N9; Fig. 1). Sites N1 and N2 are located on the grounded Larter and Lucchitta Glaciers, respectively; sites N3 and N4 are on the floating ice shelf within the N-PIIS1 region; site N5 is on an unnamed glacier; site N6 lies within the N-PIIS2 region; and sites N7–N9 are located on the Velasco Glacier.

2.3 Pinning points

We used Landsat-5/7/8 optical imagery (30 m) to identify long-term changes in the surface expression of pinning points in 1997, 2003, 2007, and 2026, following the method of Miles and Bingham (2024). We further applied the double-differential InSAR (DDInSAR) technique to track continuous pinning-point evolution from 2017–2025 (Rignot et al.,

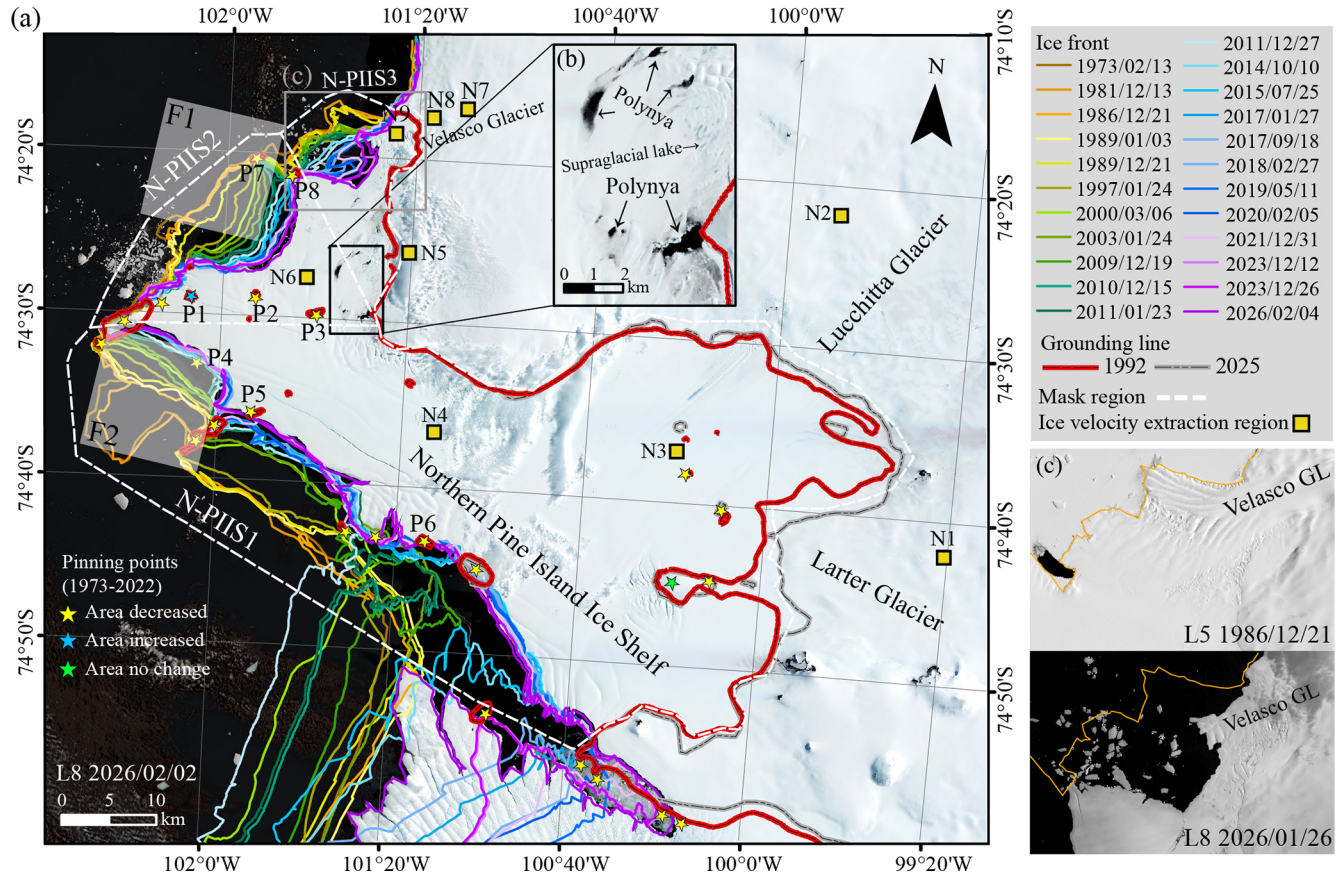


Figure 1. Location and geometry of the N-PIIS. **(a)** Overview map of the N-PIIS. The background is a Landsat-8 panchromatic image acquired on 2 February 2026, showing the extent of the northern ice shelf and its tributary glaciers. N-PIIS1, N-PIIS2, and N-PIIS3 denote ice-shelf masks used to calculate area anomalies. Points N1–N9 indicate locations of extracted ice velocity time series. Ice front positions were delineated from Landsat optical and Sentinel-1 SAR images, following Chien et al. (2025a, b). Grounding lines for 1992 (red) and 2025 (grey) are from Rignot et al. (2016) and Rignot et al. (2026), respectively. Changes in pinning points between 1973 and 2022 (stars) are from Miles and Bingham (2024). The black frame indicates the region shown in panel **(b)**, while the grey frame outlines the region in panel **(c)**. **(b)** Subregion highlighting polynya, with a Landsat-8 image acquired on 2 February 2026 as the background. **(c)** Ice-front changes at the Velasco Glacier, comparing Landsat-5 imagery from 21 December 1986 and Landsat-8 imagery from 26 January 2026.

2011). DDInSAR interferograms were generated from three-pass Sentinel-1A/B IW acquisitions with a 6 and 12 d repeat cycle between 2017 and 2025. Assuming constant ice velocity over the temporal baseline, the resulting interferograms isolate tidal flexure signals at the grounding zone, which appear as dense fringe belts. The landward limit of the fringe belt was manually digitized as the grounding line, while changes in fringe geometry were used to identify the appearance or disappearance of pinning points. All interferograms were geocoded using the REMA 200 m digital elevation model and analysed at a 20 m grid spacing (Howat et al., 2019, 2022).

2.4 Surface elevation

Surface elevation changes were assessed using ICESat-2 ATL06 land-ice height data (Smith et al., 2019, 2023) from 2019–2025. A single repeat track (track 1026) crossing the N-PIIS and adjacent polynya regions was analysed. The ICESat-2 elevations were referenced to the EGM2008 geoid, with corrections applied for ocean tides, mean dynamic topography, and the inverse barometer effect. After these corrections, we extracted the mean sea level within the same track and converted the results to heights relative to the instantaneous sea surface.

2.5 Landfast sea ice time series and SMOS thin sea ice thickness

To assess landfast sea-ice formation near the front of the N-PIIS, we used the landfast sea-ice product provided by Fraser et al. (2020a, b) to extract a time series from 2000–2018, and combined it with daily Soil Moisture and Ocean Salinity (SMOS) thin sea-ice thickness data from 2015–2026 (Huntemann et al., 2014). Due to the coarse spatial resolution (12.5 km × 12.5 km) and a detection limit of ∼ 50 cm,

the SMOS data were primarily used to confirm the presence of sea ice near the ice front. Sea-ice thickness was extracted within two predefined boxes (F1 and F2 in Fig. 1a) to monitor its temporal evolution. For consistency, we assigned a value of 51 cm to the landfast sea-ice product when landfast ice was present, matching the maximum thickness represented in the SMOS thin sea ice dataset.

3 Results

3.1 Area and ice velocity changes at the N-PIIS

The ice fronts of the N-PIIS and the Velasco Glacier have undergone multiple phases of retreat since 1973 (Fig. 1). In the N-PIIS1 region, the ice-shelf area decreased by $\sim 600\,km^2$ ($\sim 150\,\%$ of N-PIIS1 maximum area) between 1973 and 2026, with the largest loss ($\sim 200\,km^2$, $\sim 50\,\%$ loss of N-PIIS1 maximum area) occurring between 2014 and 2015, coinciding with its disconnection from the central ice shelf. The ice front in the N-PIIS1 region is now buttressed by P5 and P6 pinning points along its margin (Figs. 1a and 2a). In the N-PIIS2 region, the area decreased by $\sim 120\,km^2$ ($\sim 150\,\%$ loss of N-PIIS2 maximum area) over the same period, showing a pronounced retreat after 1986 (Fig. 2a). The N-PIIS3 region experienced a more marked retreat after 2007, with a total loss of $\sim 40\,km^2$ ($\sim 200\,\%$ loss of N-PIIS3 maximum area) (Fig. 2a). There are two pinning points P7 and P8 separating N-PIIS2 and N-PIIS3. Prior to 23 January 2011, the ice front was connected to the pinning point P7. Following a calving event between 23 January 2011 and 27 December 2011, the ice front retreated to the pinning point P8 (Fig. 1a). Comparison with the SMOS thin sea ice thickness time series indicates that calving events in the N-PIIS2 and N-PIIS3 regions increased during periods when sea ice thickness approached zero, indicating the absence of sea ice near the ice front (red semi-transparent blocks in Fig. 2a).

Ice-velocity time series at locations N1 (grounded ice region of the Larter Glacier), N2 (grounded ice region of the Lucchitta Glacier), and N3–N4 (floating region at N-PIIS1) show a general increase in annual ice velocity between 2014 and 2026, of approximately 50–100 $m\,yr^{-1}$ (Fig. 2b). In contrast, ice velocity at N5 and N6 remained relatively stable at 50–70 $m\,yr^{-1}$ over the same period. At the grounded ice region of the Velasco Glacier (N7), ice velocity increased from 2014–2022, decreased from 2022–2024, and increased again after 2024. At the floating region (N8 and N9), ice velocity increased from 2014–2021, decreased from 2021–2024, and increased again after 2024 (Fig. 2b).

Here we present two representative calving events that occurred following sea-ice loss (particularly landfast sea-ice loss). The first occurred at the Velasco Glacier during 14–17 January 2022 (Fig. 3), and the second occurred at the N-PIIS2 and N-PIIS3 region after November 2025 (Fig. 4). For the 2022 calving event at the Velasco Glacier, a rift was first observed in 14 September 2021, coinciding with the formation of a polynya. The polynya expanded, and new fractures formed within the fast ice on 10 November 2021. Fast-ice breakup progressed by 28 November 2021, propagating toward the ice tongue, and complete disintegration was observed by 20 December 2021 as the polynya further expanded. The calving event ultimately detached an iceberg of approximately $3.50\,km^2$.

Figure 4 shows the sea-ice conditions and ice-shelf calving events at N-PIIS2 and N-PIIS3 after October 2025, and compares the area loss between 28 November 2025 and 24 March 2026. The landfast sea ice almost completely broke up near the N-PIIS2 and N-PIIS3 regions after 28 November 2025 (Fig. 4b). Following this breakup, several calving events occurred between December 2025 and March 2026, leading to a reduction in ice-shelf area (Fig. 4c–e). However, the area of the region near pinning point P8 does not change so much. The Velasco Glacier front also calved during this period (Fig. 4c).

In Fig. 4a, several polynyas are identified within the N-PIIS, and their spatial and temporal evolution from 1986–2026 is shown in Fig. 5. Polynyas are not detectable in the Landsat images acquired on 21 December 1986, 21 December 1989, and 24 January 1997 (Fig. 5a), although these images reveal notable surface changes in the region. The ice surface appears smoother in 1986 than in 1997, and supraglacial lakes are also observed in 1997. Polynyas were clearly detected in 2003, 2005, 2007, 2019, 2020, 2021, 2022, and 2026 (Fig. 5a–c and e), with a marked area expansion observed in 2021 and 2026 relative to earlier years. During the austral summer, supraglacial lakes form first, followed by the development of polynyas in the same regions (Fig. 5b4–b6, c, and d). In the austral winter of 2024, areas of reduced backscatter are identified in Sentinel-1 imagery (Fig. 5b). Combined with ICESat-2 surface elevation data, these regions exhibit a continuous decrease in elevation (Fig. 6). Furthermore, surface elevation in the N-PIIS1 region (approximately 50 m) is higher than in the N-PIIS2 and N-PIIS3 regions (less than 15 m), suggesting that ice thickness in N-PIIS1 is greater than in the other two regions (Fig. 6).

3.2 Pinning-point changes and rift propagation at the N-PIIS

The pinning-point dataset from Miles and Bingham (2024) indicates that the area of most pinning points on the N-PIIS decreased continuously from 1973–2022 (Fig. 1a), suggesting sustained ice thinning in this region. Building on this, we use Landsat-5/7/8 optical imagery to investigate the long-term evolution of pinning points on the N-PIIS (Fig. 7). Pinning points P1, P2, and P3 persist from 1997–2026, whereas P4 no longer detectable by 2026 following nearby calving events, and P5 also no longer detectable after 2007.

Double-difference interferograms derived from the DDInSAR method reveal temporal variations in pinning-point ex-

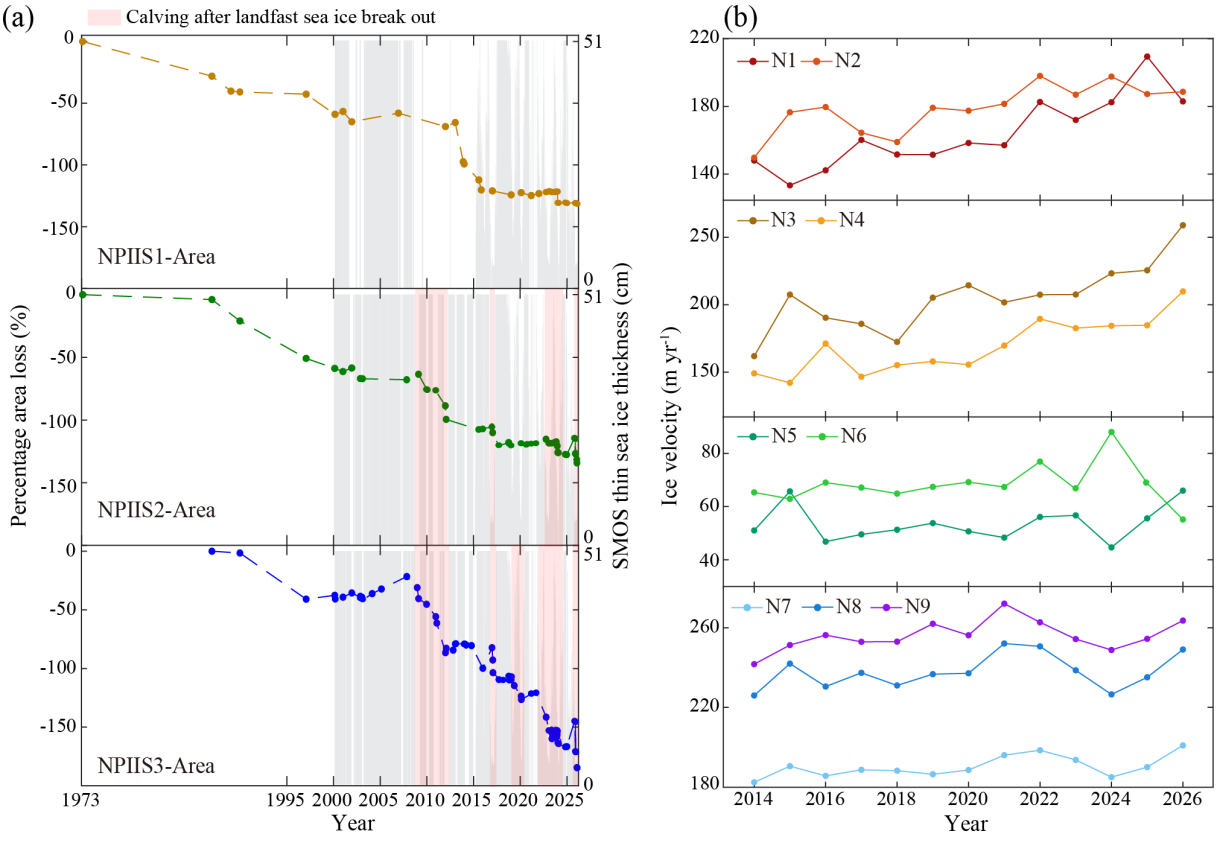


Figure 2. Time series of area anomalies, SMOS thin sea-ice thickness, and ice velocity. **(a)** Percentage area loss time series for the N-PIIS from 1973–2026, together with SMOS thin sea-ice thickness from 2000–2026. Blue bars represent SMOS thin sea-ice thickness, and red frames denote calving events that occurred following landfast sea-ice breakup. **(b)** Ice velocity time series at locations N1–N9.

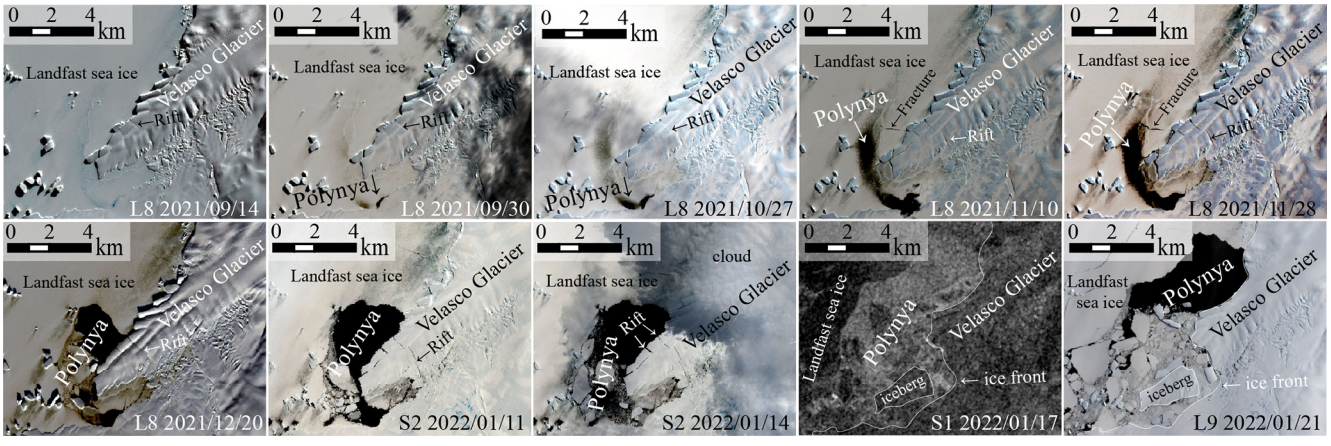


Figure 3. The 2022 calving event at the Velasco Glacier as documented by Landsat-8/9 and Sentinel-1/2 imagery from September 2021–January 2022.

tent under tidal forcing. Interferograms from August 2017–December 2025 illustrate the evolution of P1–P6. P1 remains present throughout the entire period. P2 exhibits the largest variability and is clearly detectable from 2017 to November 2020 (Fig. 8), with maximum interferometric fringe extent between March and June 2020 (Fig. 8d1 and 8d2). Since January 2021, P2 appears intermittently, and its centre gradually migrates southward, currently lying south of a rift formed in 2025 (Fig. 9). P3 is no longer detectable after October 2022 (Fig. 9b2), while P4 is not detected at any time dur-

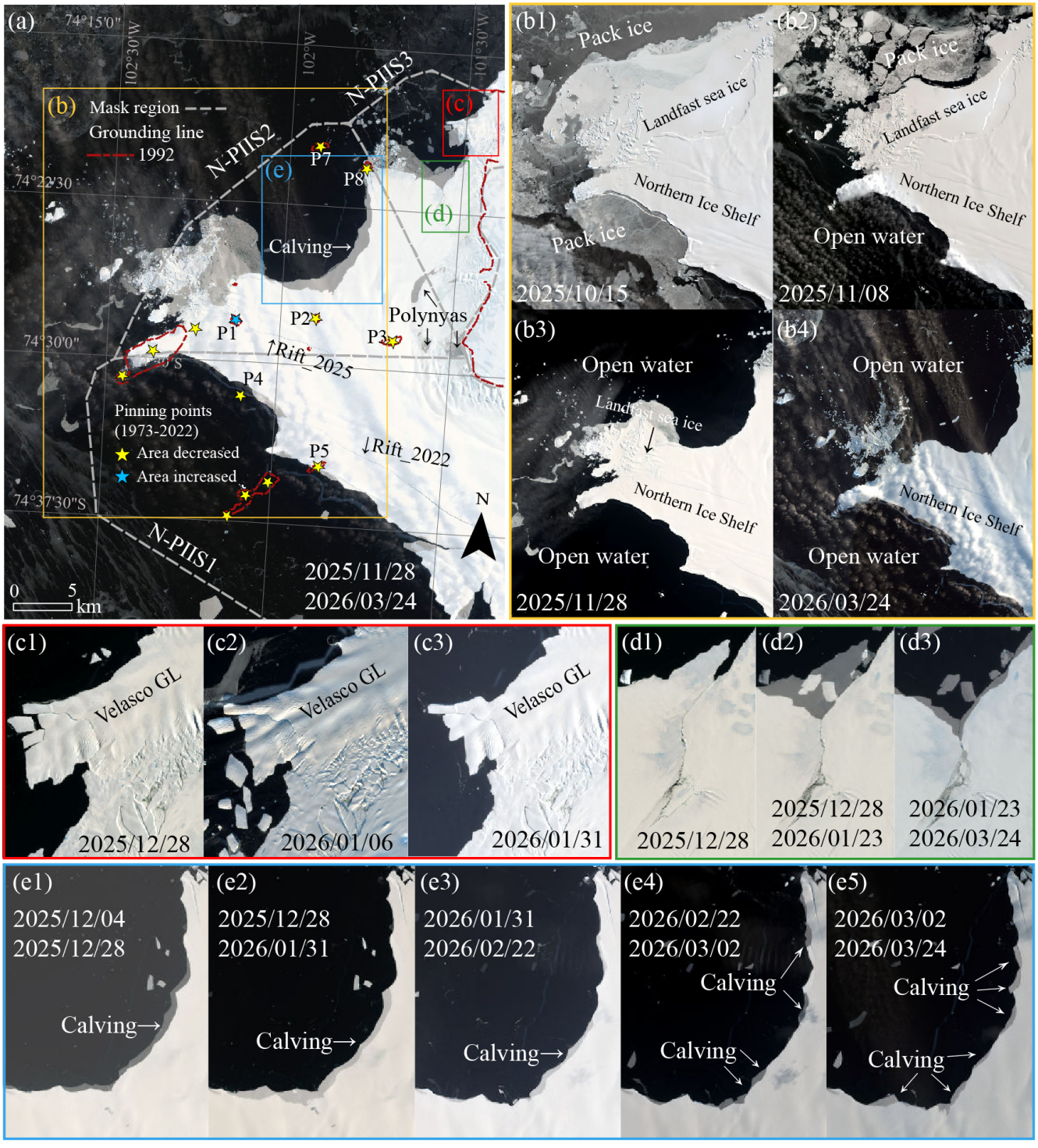


Figure 4. Overview of changes in the N-PIIS and its surrounding sea area from October 2025–March 2026. **(a)** Changes in the area of the N-PIIS between 28 November 2025 and 24 March 2026. Pinning points (stars) are from Miles and Bingham (2024). The white dashed line indicates the ice-shelf mask. The 1992 grounding line is from Rignot et al. (2016). **(b)** Overview of fast-ice changes from 15 October 2025–24 March 2026. **(c)** Calving events at the Velasco Glacier between 28 December 2025 and 31 January 2026. **(d)** Calving events at the N-PIIS between 28 December 2025 and 24 March 2026. **(e)** Calving events at the N-PIIS between 4 December 2025 and 24 March 2026. All optical satellite images used in this figure are from Sentinel-2.

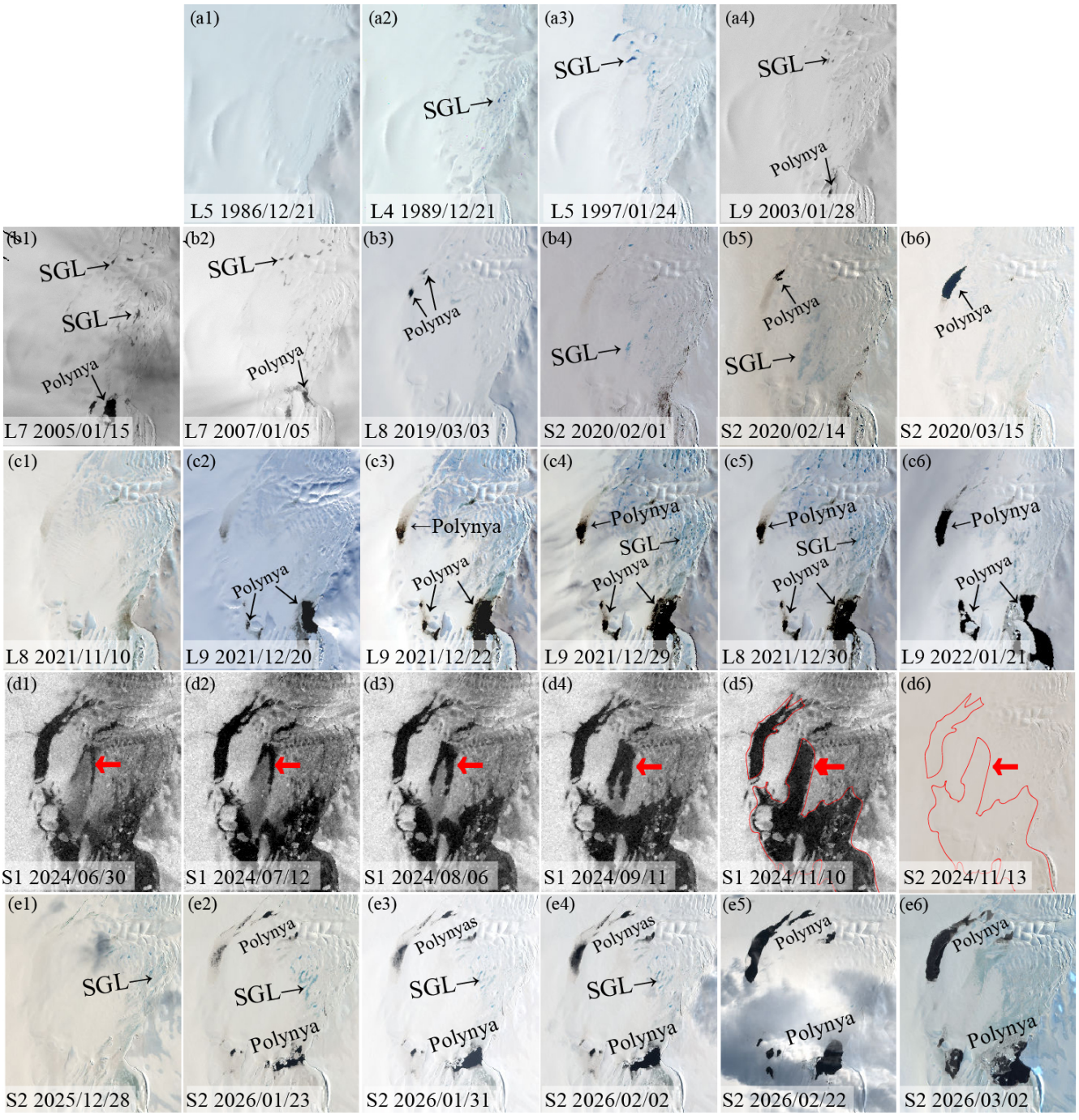


Figure 5. Distribution and development of polynyas and supraglacial lakes (SGL) within the N-PIIS. **(a)** Overview map in 1986, 1989, 1997, and 2003. **(b)** Overview map in 2005, 2007, 2019, and 2020. **(c)** Overview of polynya development during the 2021/2022 austral summer. **(d)** Decrease in backscatter coefficient observed in Sentinel-1 imagery from June to November 2024 (red arrows). **(e)** Overview of polynya development during the 2025/2026 austral summer.

ing 2017–2025. P5 begins to disappear in December 2023, likely due to ice-shelf calving after April 2023 that led to a loss of contact with the pinning point. Deformation associated with basal-channel development is also evident in the interferograms (Figs. 8 and 9).

In Fig. 7d, pinning points P2 and P3 are located close to a newly formed rift in 2025, while P4 and P5 are near a rift that developed in 2022. The 2025 rift initiated north of pinning point P2 between June and August 2025 (Fig. 10c) and extended rapidly within less than one year, increasing from ap-

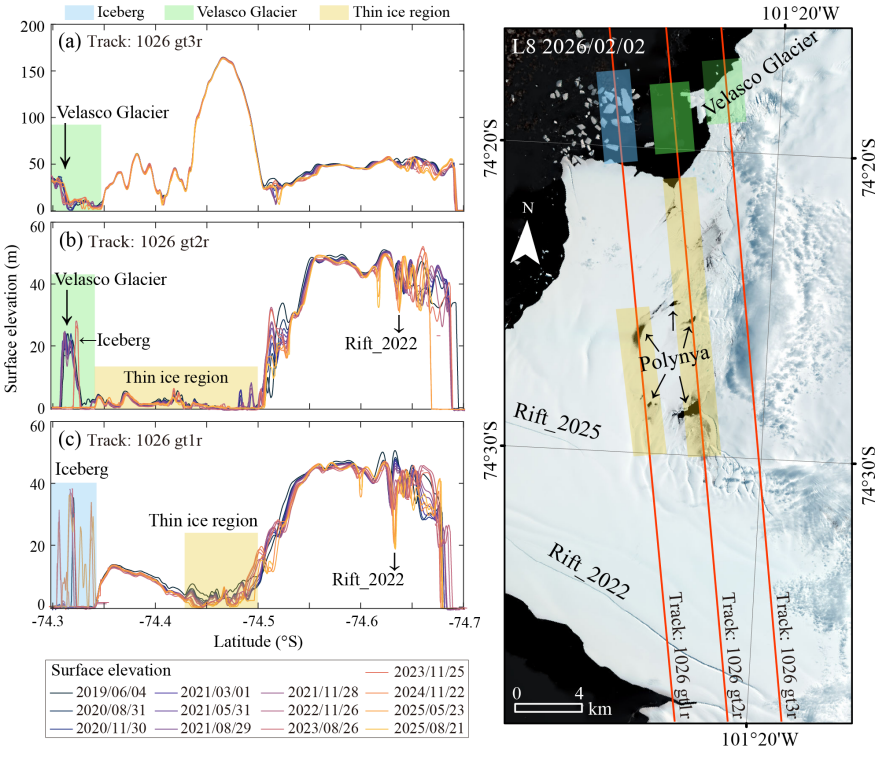


Figure 6. ICESat-2 ground tracks and surface elevation profiles at the N-PIIS. Panels **(a–c)** show surface elevation profiles along each beam over the latitude from 74.3–74.7° S. Semi-transparent coloured bands highlight surface elevation over the Velasco Glacier (green), thin ice regions (yellow), and icebergs (blue). Panel **(d)** shows the Locations of the three strong beams (gt1r, gt2r, gt3r) from ICESat-2 track 1026. Coloured bands in **(a–c)** correspond to the same regions indicated in (d).

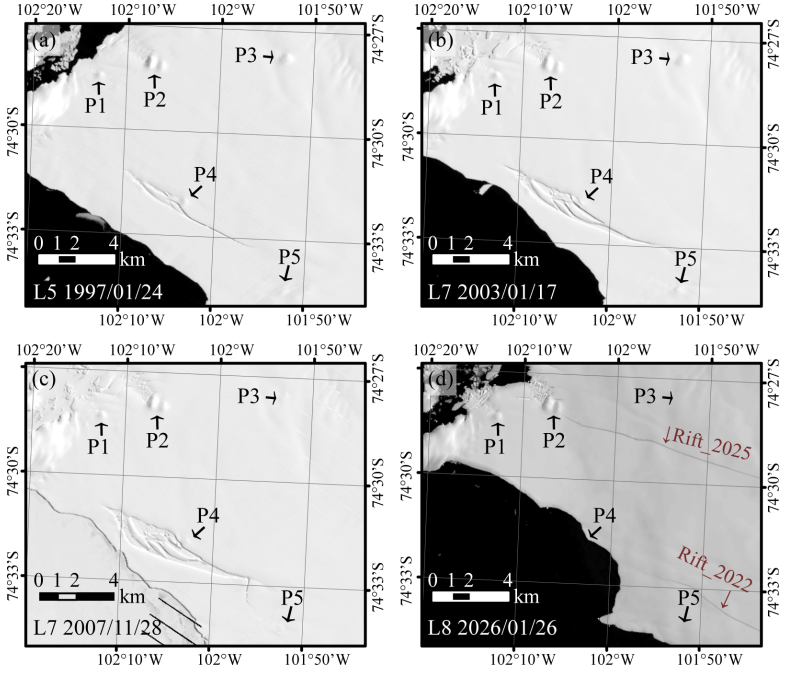


Figure 7. Changes in pinning points in Landsat imagery. Panels **(a–d)** show pinning-point conditions on 24 January 1997 (Landsat-5), 17 January 2003 (Landsat-7), 28 November 2007 (Landsat-7), and 26 January 2026 (Landsat-8), respectively. Panel **(d)** also reveals the positions of rifts that appeared in 2022 (Rift_2022) and 2025 (Rift_2025).



Figure 8. Changes in pinning points P1, P2, P3, and P5 derived from double-difference interferograms over the N-PIIS from 2017–2020. Panels **(a–d)** show results for 2017, 2018, 2019, and 2020, respectively.

proximately 4.1 km on 26 June 2025 to 12.5 km on 29 March 2026, an elongation of 8.4 km (Fig. 10b).

In comparison, the rift that developed in 2022 shows a marked change in propagation rate (Fig. 11a). Between 2022 and 2024, the rift length increased at a rate of approximately 4 km yr^{-1} (from 4.5 km on 14 December 2022 to 8.5 km on 21 December 2023, and to 11.3 km on 27 December 2024). However, from 27 December 2024–28 December 2025, the rift length increased from 11.3–19.5 km, corresponding to a growth rate of approximately 8 km yr^{-1}, nearly twice the earlier rate. Double-difference interferograms reveal deformation in this region and indicate the presence of pinning points near the rift propagation area (Fig. 11b).

The double-difference interferograms from 2017–2025 further reveal the evolution of pinning points near the 2022 rift (Figs. 12 and 13). A rift is already present near P5 in August 2017 (Fig. 12a1). Following a calving event in April 2020, the area of P5 decreases significantly (Fig. 12d1), and after further ice-shelf breakup in April 2023, it disappears completely (Fig. 13b4). The rift that emerged in 2022 initiated near pinning point P6 and propagated toward the location of P5 (Fig. 13c3).

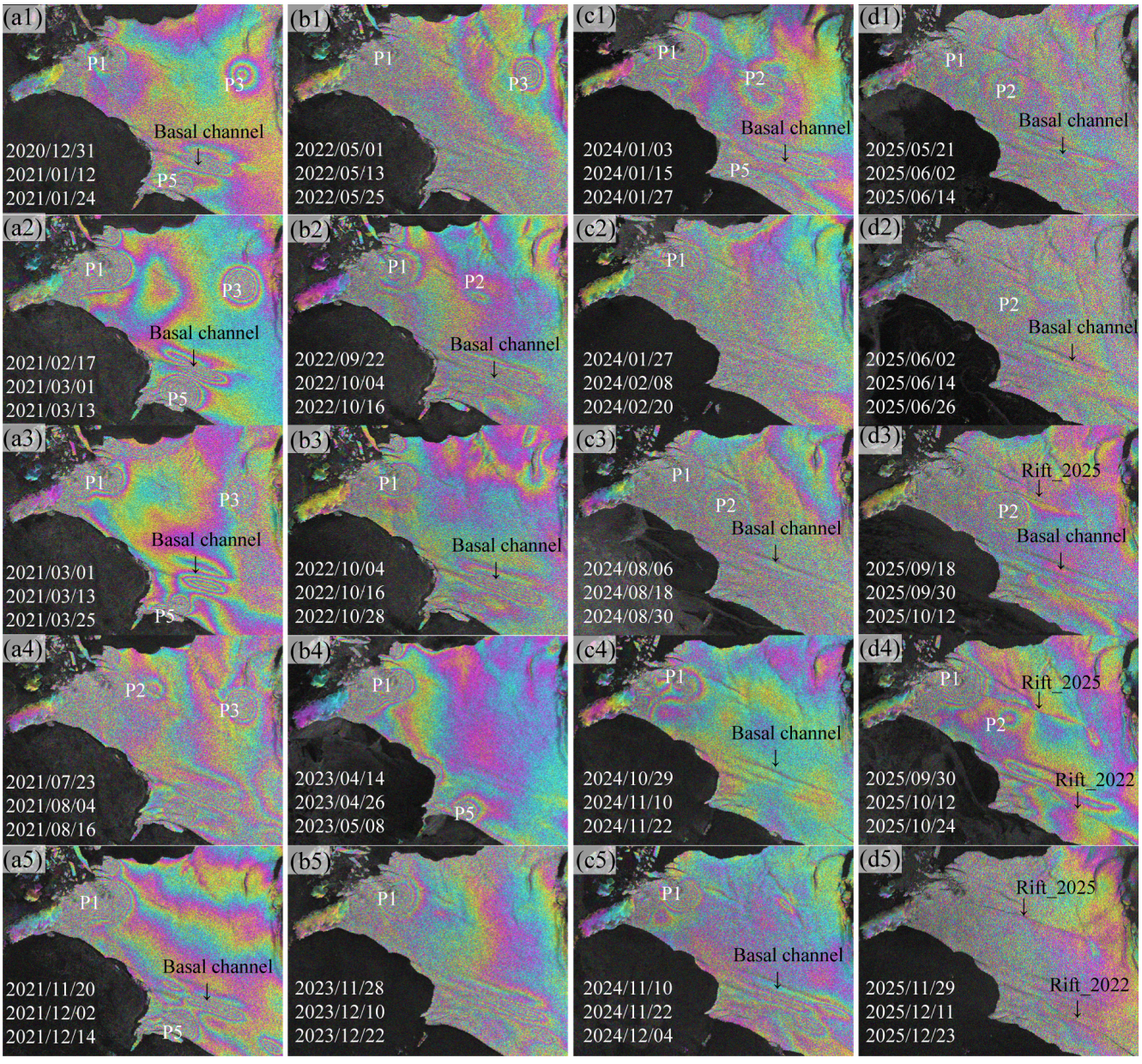


Figure 9. Changes in pinning points P1, P2, P3, and P5 derived from double-difference interferograms over the N-PIIS from 2021–2025. Panels **(a–d)** show results for 2021, 2022, 2023, 2024, and 2025, respectively.

4 Discussion

4.1 Influence of landfast sea-ice breakup and pinning-point loss on calving and ice velocity changes of the N-PIIS

The ice front of the N-PIIS has retreated continuously since 1973, with a marked reduction in ice-shelf area following the loss of contact with pinning points (Fig. 1a). Time series of ice-shelf area anomalies and SMOS thin sea-ice thickness indicate that pronounced ice-front retreat occurs during periods of reduced thin sea ice (i.e., absence of landfast ice), particularly in the N-PIIS2 and N-PIIS3 regions (Fig. 2a). This relationship is further supported by the 2021 calving event at the Velasco Glacier, which occurred following polynya formation and landfast sea-ice breakup (Fig. 3), as well as by calving events between November 2025 and March 2026 that followed the loss of landfast ice in the N-PIIS2 and N-PIIS3 regions (Fig. 4).

In contrast, the N-PIIS1 region, where the ice front is supported by multiple pinning points and sheltered within Pine Island Bay, shows no significant calving during open-water periods (Fig. 1a). ICESat-2 elevation data (Fig. 6) indicate

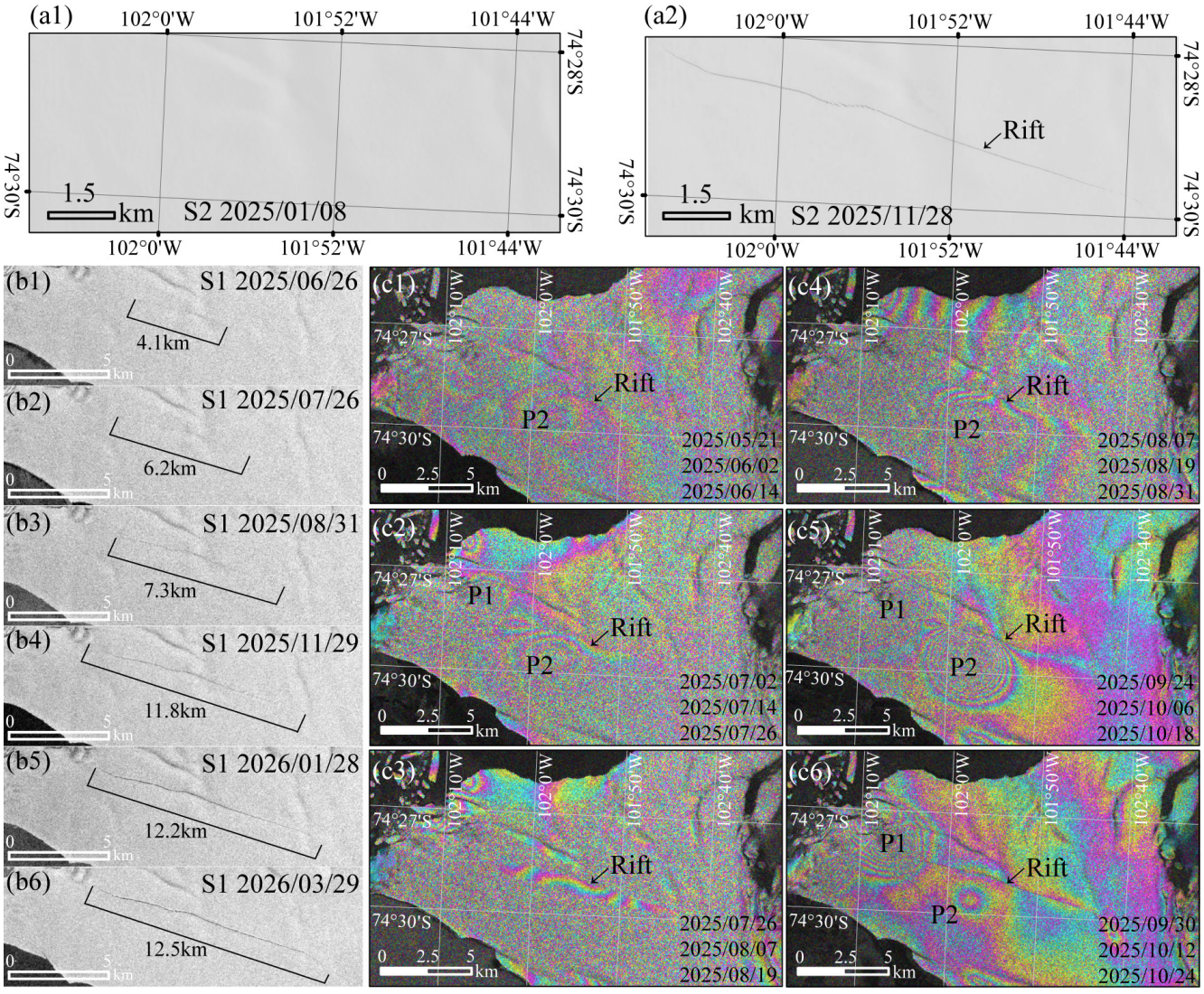


Figure 10. Development of the new rift in 2025 and corresponding double-difference interferograms. **(a1, a2)** Sentinel-2 images on 8 January 2025 and 28 November 2025, respectively. **(b)** Rift propagation from 26 June 2025–29 March 2026 derived from Sentinel-1 SAR imagery. **(c)** Double-difference interferograms from May–October 2025.

surface elevations of ∼ 50 m in N-PIIS1, compared to < 15 m in N-PIIS2 and N-PIIS3. The firn air content in this region is approximately 20 m. Accordingly, the ice thickness at N-PIIS1 is about 300 m, while the ice thickness at N-PIIS2 and N-PIIS3 is less than 150 m. These observations are consistent with modelling results (Teder et al., 2025), which suggest that flexural stresses induced by ocean swell more strongly affect thinner ice shelves (< 150 m). This implies that ocean swell may contribute to calving in N-PIIS2 and N-PIIS3, which are directly exposed to the Amundsen Sea. Accordingly, the Pine Island Ice Shelf should be considered as three sub-regions (northern, central, and southern) when assessing the influence of ocean forcing on ice-shelf stability.

Annual ice-velocity changes indicate that most of the study region, including both grounded and floating ice, is accelerating. Ice velocities at N5 and N6 are lower than in other regions, suggesting that if this area were to be lost, a long recovery time would be required for re-establishment of its present configuration. At the Velasco Glacier, a polynya formed in October 2021, followed by a calving event at the glacier front in January 2022. However, no clear increase in ice velocity was observed following this event, suggesting that the associated loss of floating ice area did not substantially alter the buttressing of the grounded glacier at that time. In contrast, the area of N-PIIS3 decreased substantially after 2024, resulting in the loss of contact between the Velasco Glacier and N-PIIS3 (Movie S1 in the Supplement). Ice velocity at the Velasco Glacier increased during the same period. This temporal correspondence suggests that the loss of the N-PIIS3 connection may have contributed to the observed

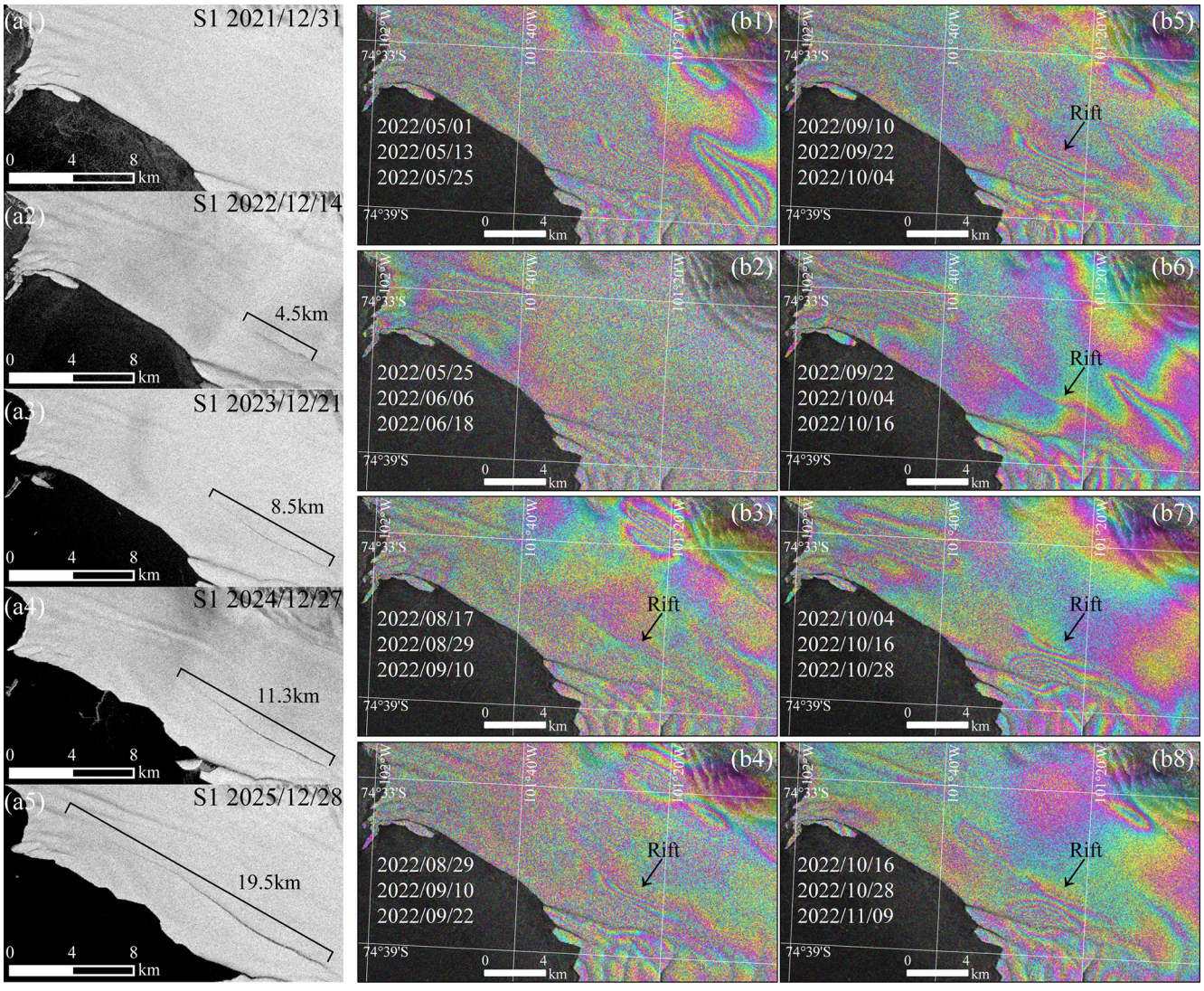


Figure 11. Development of the 2022 rift and corresponding double-difference interferograms. **(a)** Rift propagation from 31 December 2021–28 December 2025 derived from Sentinel-1 SAR imagery. **(b)** Double-difference interferograms from May–October 2022.

velocity increase at the Velasco Glacier, although other factors may also have influenced its dynamic response. Further studies are needed to quantify the relative contributions of ice-shelf area loss, changes in pinning-point support, sea-ice conditions, and other factors to the observed changes in ice velocity.

4.2 Ice thinning, pinning-point loss, and rift propagation

The occurrence of polynyas, decreasing surface elevation, southward migration of pinning point P2, and the disappearance of P3 and P4 collectively indicate ongoing thinning of the N-PIIS (Figs. 6–13). The loss of pinning points and the formation of a polynya within the ice shelf are consistent with regional thinning and may have facilitated the progressive disconnection of the ice shelf from the grounded ice sheet. The formation of a polynya may alter local air-ocean heat exchange and indicate enhanced oceanic heat reaching the surface, potentially contributing to ice-shelf basal melt and fracture (Savidge et al., 2023). The presence and distribution of pinning points near both ends of the rifts that developed in 2022 and 2025 may indicate changes in the interaction between the ice-shelf base and the underlying bedrock (Figs. 7–13).

The loss of pinning points reduces local buttressing, alters internal stress distributions, and promotes rift propagation (Arndt et al., 2018; Benn et al., 2022). The spatial correspondence between rift development and pinning-point evolution further suggests that thinning-driven ephemeral grounding could plays a key role in the formation of new rifts during the austral winters of 2022 and 2025 (Figs. 10 and 11).

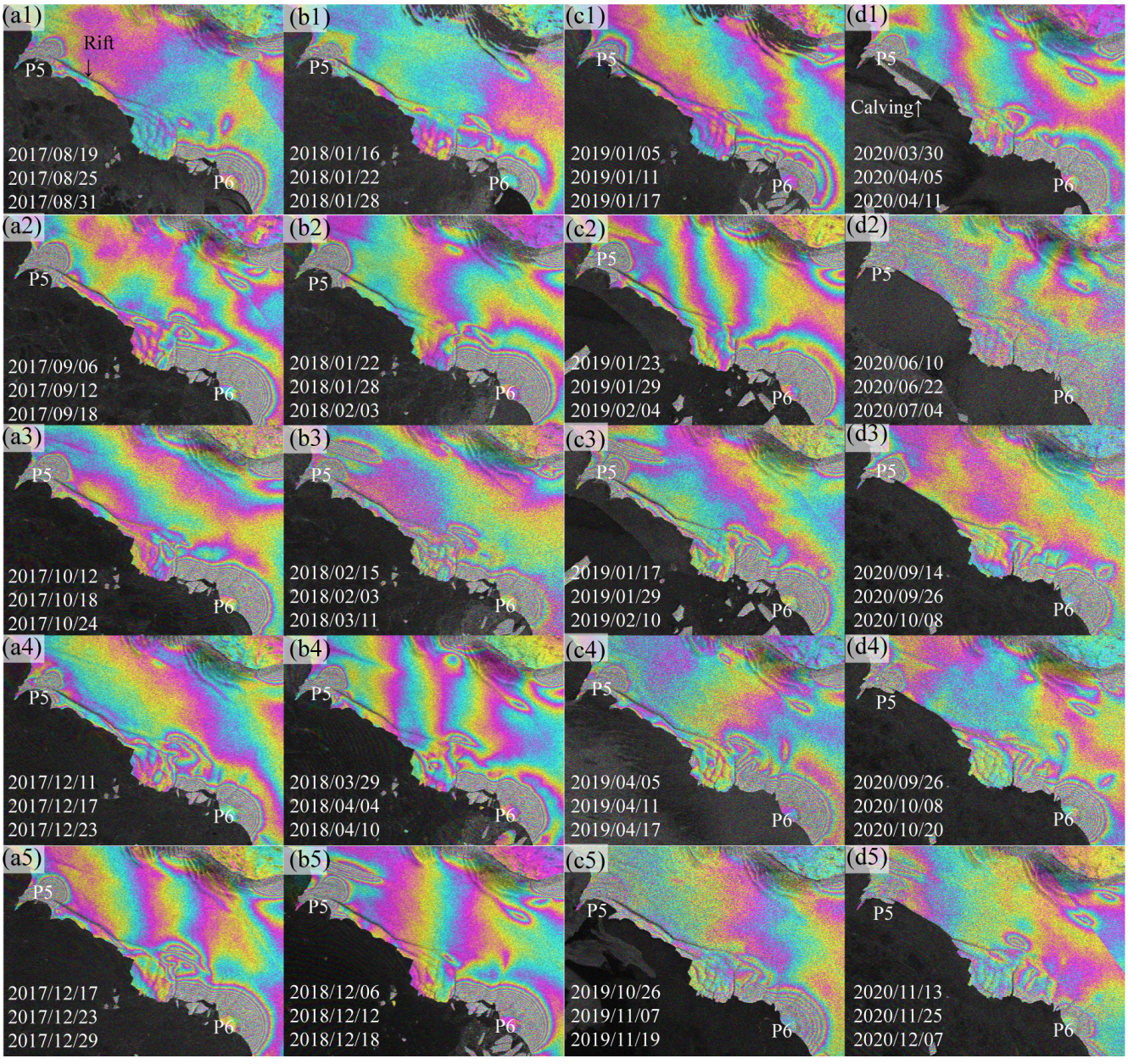


Figure 12. Double-difference interferograms of the N-PIIS from 2017–2020. Panels **(a–d)** show results for 2017, 2018, 2019, and 2020, respectively.

The observed ice thinning, loss of pinning points, and propagation of new rifts suggest that the N-PIIS may be undergoing changes that could decrease its stability to further dynamic evolution. Although large-scale collapse has not yet occurred, continued thinning and the loss of pinning points may influence ice-shelf stability, while changes in sea-ice conditions may alter the exposure of the ice-shelf front to ocean swell and associated flexural stresses, potentially affecting further rift propagation and ice-shelf calving. Sustained satellite observations, together with in situ measurements and numerical modelling, are therefore needed to better constrain the relative contributions of these processes and assess the potential for further rift propagation and large-scale ice-shelf change.

5 Conclusions

Using satellite imagery and datasets, we investigated recent changes in the N-PIIS and documented ongoing calving, thinning, and ungrounding. Since 1973, the area of the N-PIIS has decreased, while ice velocities have increased. The

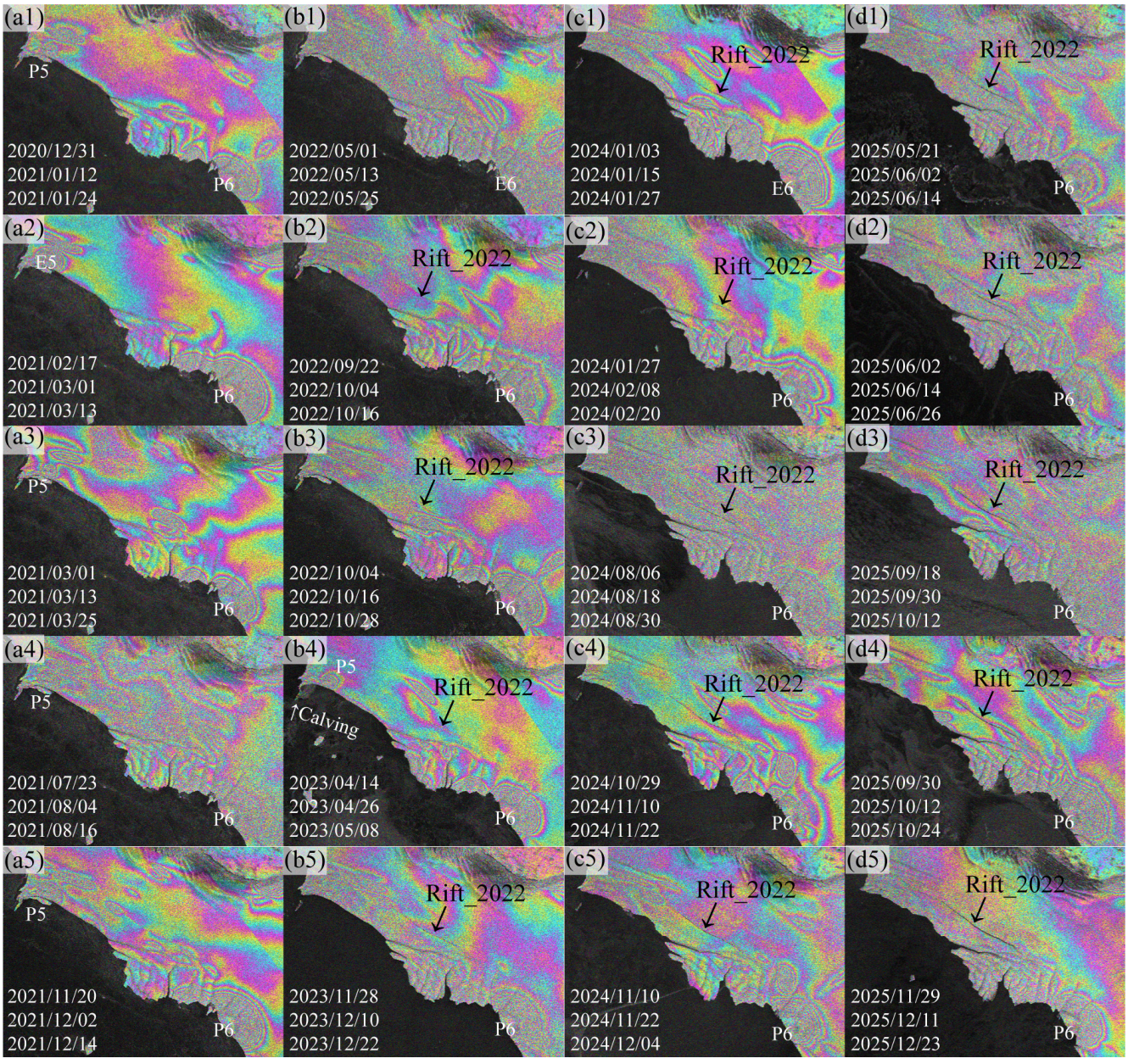


Figure 13. Double-difference interferograms of the N-PIIS from 2021–2025. Panels **(a–d)** show results for 2021, 2022, 2023, 2024, and 2025, respectively.

loss of pinning points, together with ICESat-2 surface elevation data, indicates sustained ice thinning. Polynya formed within the ice shelf may promote disconnection from the ice sheet. Observations of calving after November 2025, the development of new rifts since the austral winter of 2022 and 2025, and continued thinning provide a comprehensive record of recent dynamic changes in this region. Continued monitoring through satellite observations, in situ measurements, and numerical modelling, will be critical to determine whether ongoing thinning, calving, and rift propagation may lead to more rapid structural changes in the future.

Code and data availability. All software (except GAMMA, which is commercial software and was used to generate DDInSAR interferograms), codes, and satellite imagery used in this study are publicly available and can be obtained from the following sources: Processed area shape files, ICESat-2 data, and related MATLAB scripts for plotting figures are available from Zenodo (Chien et al., 2026). The MATLAB plotting codes on which this article is based are available in Greene et al. (2017) and Greene (2021). REMA 200 m DEM mosaic is available from Howat et al. (2022). Ice front positions were delineated from Landsat optical imagery and Sentinel-1 SAR data, and are available from Zenodo (Chien et al., 2025b). Grounding line positions were obtained

from NSIDC (Rignot et al., 2016). Pinning points were sourced from Miles and Bingham (2024). Optical and SAR imagery from Landsat, Sentinel-1, and Sentinel-2 were accessed via USGS EarthExplorer (https://earthexplorer.usgs.gov/, last access: 15 January 2026), Google Earth Engine (https://earthengine.google.com/, last access: 15 January 2026), and the Copernicus Data Space Browser (https://browser.dataspace.copernicus.eu/, last access: 15 January 2026). ICESat-2 ATL06 surface elevation data are available from NSIDC (Smith et al., 2023). The Sentinel-1 image IDs used for the DDInSAR analysis can be accessed in Supplementary Table S1.

Supplement. The supplement related to this article is available online at https://doi.org/10.5194/tc-20-6071-2026-supplement.

Author contributions. YC and CZ designed the experiments and YC developed the MATLAB code and performed all the experiments. YC prepared the manuscript supervised from CZ and BZ.

Competing interests. The contact author has declared that none of the authors has any competing interests.

Disclaimer. Publisher's note: Copernicus Publications remains neutral with regard to jurisdictional claims made in the text, published maps, institutional affiliations, or any other geographical representation in this paper. The authors bear the ultimate responsibility for providing appropriate place names. Views expressed in the text are those of the authors and do not necessarily reflect the views of the publisher.

Acknowledgements. The authors thank the organizations and projects listed in the Data Availability section for providing essential datasets. We are also grateful to the anonymous reviewers and the scientific editor for their constructive comments, which greatly improved the manuscript.

Financial support. This research was supported by the National Natural Science Foundation of China (Grants 42171133 and 41941010), the Fundamental Research Funds for the Central Universities (Grant 2042024kf0016), and the National Science and Technology Council of Taiwan (Grant 115-2811-M-008-035).

Review statement. This paper was edited by Sheng Fan and reviewed by two anonymous referees.

References

Andersen, J. K., Millan, R., Rignot, E., Gimenes, L., Scheuchl, B., Barré, J. B., and Bjørk, A. A.: Brief communication: Updated grounding line mapping in the Amundsen Sea Embayment, Antarctica, from one day repeat Sentinel-1 SAR data, The Cryosphere, 20, 1589–1598, https://doi.org/10.5194/tc-20-1589-2026, 2026.

Arndt, J. E., Larter, R. D., Friedl, P., Gohl, K., Höppner, K., and the Science Team of Expedition PS104: Bathymetric controls on calving processes at Pine Island Glacier, The Cryosphere, 12, 2039–2050, https://doi.org/10.5194/tc-12-2039-2018, 2018.

Benn, D. I., Luckman, A., Åström, J. A., Crawford, A. J., Cornford, S. L., Bevan, S. L., Zwinger, T., Gladstone, R., Alley, K., Pettit, E., and Bassis, J.: Rapid fragmentation of Thwaites Eastern Ice Shelf, The Cryosphere, 16, 2545–2564, https://doi.org/10.5194/tc-16-2545-2022, 2022.

Chien, Y., Zhou, C., and Riel, B.: Mélange-driven coupling between the central Pine Island Ice Shelf and the Piglet Glacier reverses recent acceleration trends, Geophys. Res. Lett., 52, e2025GL119556, https://doi.org/10.1029/2025GL119556, 2025a.

Chien, Y., Zhou, C., and Riel, B.: Datasets for the study "Mélange-driven coupling between the central Pine Island Ice Shelf and the Piglet Glacier reverses recent acceleration trends", Zenodo [data set], https://zenodo.org/uploads/17722558 (last access: 15 January 2026), 2025b.

Chien, Y., Zhou, C., and Zhang, B.: Dataset for the manuscript "Progressive Changes in Geometry and Dynamics of the Northern Pine Island Ice Shelf, West Antarctica", Zenodo [data set], https://doi.org/10.5281/zenodo.22044739 (last access: 7 October 2026), 2026.

Dutrieux, P., De Rydt, J., Jenkins, A., Holland, P. R., Ha, H. K., Lee, S. H., Steig, E. J., Ding, Q., Abrahamsen, E. P., and Schröder, M.: Strong Sensitivity of Pine Island Ice-Shelf Melting to Climatic Variability, Science, 343, 174–178, https://doi.org/10.1126/science.1244341, 2014.

Fahnestock, J. R. and Dow, D. E.: Mappin: A web-native browse tool for the NASA JPL ITS_LIVE project's ice velocity dataset, in: 2023 IEEE 14th Annual Ubiquitous Computing, Electronics and Mobile Communication Conference (UEMCON), IEEE, 97–100, https://doi.org/10.1109/UEMCON59035.2023.10316074, 2023.

Fraser, A. D., Massom, R. A., Ohshima, K. I., Willmes, S., Kappes, P. J., Cartwright, J., and Porter-Smith, R.: High-resolution mapping of circum-Antarctic landfast sea ice distribution, 2000–2018, Earth Syst. Sci. Data, 12, 2987–2999, https://doi.org/10.5194/essd-12-2987-2020, 2020a.

Fraser, A. D., Massom, R. A., Ohshima, K. I., Willmes, S., Kappes, P., Cartwright, J., and Porter-Smith, R.: Circum-Antarctic landfast sea-ice extent, 2000–2018, Australian Antarctic Data Centre, https://doi.org/10.26179/5d267d1ceb60c, 2020b.

Gardner, A. S., Greene, C. A., Kennedy, J. H., Fahnestock, M. A., Liukis, M., López, L. A., Lei, Y., Scambos, T. A., and Dehecq, A.: ITS_LIVE global glacier velocity data in near-real time, The Cryosphere, 19, 3517–3533, https://doi.org/10.5194/tc-19-3517-2025, 2025.

Greene, C. A., Gwyther, D. E., and Blankenship, D. D.: Antarctic mapping tools for MATLAB, Comput. Geosci., 104, 151–157, https://doi.org/10.1016/j.cageo.2016.08.003, 2017.

Greene, C. A.: Antarctic Mapping Tools, Version 6, [Software], GitHub, https://github.com/chadagreene/Antarctic-Mapping-Tools (last access: 15 January 2026), 2021.

Howat, I. M., Porter, C., Smith, B. E., Noh, M.-J., and Morin, P.: The Reference Elevation Model of Antarctica, The Cryosphere, 13, 665–674, https://doi.org/10.5194/tc-13-665-2019, 2019.

Howat, I., Porter, C., Noh, M., Husby, E., Khuvis, S., Danish, E., Tomko, K., Gardiner, J., Negrete, A., Yadav, B., Klassen, J., Kelleher, C., Cloutier, M., Bakker, J., Enos, J., Arnold, G., Bauer, G., and Morin, P.: The Reference Elevation Model of Antarctica–Mosaics, Version 1.1, [data set], Harvard Dataverse, https://data.pgc.umn.edu/elev/dem/setsm/REMA/mosaic/v1.1/200m/ (last access: 15 January 2026), 2022.

Huntemann, M., Heygster, G., Kaleschke, L., Krumpen, T., Mäkynen, M., and Drusch, M.: Empirical sea ice thickness retrieval during the freeze-up period from SMOS high incident angle observations, The Cryosphere, 8, 439–451, https://doi.org/10.5194/tc-8-439-2014, 2014.

Joughin, I., Shapero, D., Smith, B., Dutrieux, P., and Barham, M.: Ice-shelf retreat drives recent Pine Island Glacier speedup, Sci. Adv., 7, eabg3080, https://doi.org/10.1126/sciadv.abg3080, 2021.

Miles, B. W. J. and Bingham, R. G.: Progressive unanchoring of Antarctic ice shelves since 1973, Nature, 626, 785–791, https://doi.org/10.1038/s41586-024-07049-0, 2024.

Rignot, E.: Ice-shelf changes in Pine Island Bay, Antarctica, 1947–2000, J. Glaciol., 48, 247–256, https://doi.org/10.3189/172756502781831386, 2002.

Rignot, E., Mouginot, J., and Scheuchl, B.: Antarctic grounding line mapping from differential satellite radar interferometry, Geophys. Res. Lett., 38, L10504, https://doi.org/10.1029/2011GL047109, 2011.

Rignot, E., Mouginot, J., and Scheuchl, B.: MEaSUREs Antarctic Grounding Line from Differential Satellite Radar Interferometry (NSIDC-0498, Version 2), NASA NSIDC DAAC [data set], https://doi.org/10.5067/IKBWW4RYHF1Q (last access: 15 January 2026), 2016.

Rignot, E., Scheuchl, B., Barre, J. B., Brancato, V., Charrier, L., Chen, H., Ciraci, E., Dinh, A., Herreid, S., Jeong, S., Li, X., Mitchell, T., Mohajerani, Y., Shamsian, S., Tolpekin, V., Velicogna, I., and Wollersheim, M.: Thirty years of glacier grounding line retreat in Antarctica, P. Natl. Acad. Sci. USA, 123, e2524380123, https://doi.org/10.1073/pnas.2524380123, 2026.

Savidge, E., Snow, T., and Siegfried, M. R.: Multi-decadal record of sensible-heat polynya variability from satellite optical and thermal imagery at Pine Island Glacier, West Antarctica, Geophys. Res. Lett., 50, e2023GL106178, https://doi.org/10.1029/2023GL106178, 2023.

Schmeltz, M., Rignot, E., and MacAyeal, D. R.: Ephemeral grounding as a signal of ice-shelf change, J. Glaciol., 47, 71–77, https://doi.org/10.3189/172756501781832502, 2001.

Smith, B., Adusumilli, S., Csathó, B. M., Felikson, D., Fricker, H. A., Gardner, A. S., Holschuh, N., Lee, J., Nilsson, J., Paolo, F., Siegfried, M. R., Sutterley, T., and the ICESat-2 Science Team: ATLAS/ICESat-2 L3A Land Ice Height, Version 6, NASA NSIDC DAAC [data set], https://doi.org/10.5067/ATLAS/ATL06.006 (last access: 15 January 2026), 2023.

Smith, B., Fricker, H. A., Holschuh, N., Gardner, A. S., Adusumilli, S., Brunt, K. M., Csatho, B., Harbeck, K., Huth, A., Neumann, T., Nilsson, J., and Siegfried, M. R.: Land ice height-retrieval algorithm for NASA's ICESat-2 photon-counting laser altimeter, Remote Sens. Environ., 233, 111352, https://doi.org/10.1016/j.rse.2019.111352, 2019.

Teder, N. J., Bennetts, L. G., Reid, P. A., Massom, R. A., Pitt, J. P. A., Scambos, T. A., and Fraser, A. D.: Large-scale ice-shelf calving events follow prolonged amplifications in flexure, Nat. Geosci., 18, 599–606, https://doi.org/10.1038/s41561-025-01713-4, 2025.

Walker, C. C., Millstein, J. D., Miles, B. W. J., Cook, S., Fraser, A. D., Colliander, A., Misra, S., Trusel, L. D., Adusumilli, S., Roberts, C., and Fricker, H. A.: Multi-decadal collapse of East Antarctica's Conger–Glenzer Ice Shelf, Nat. Geosci., 17, 1240–1248, https://doi.org/10.1038/s41561-024-01582-3, 2024.